ACSNANO

www.acsnano.org

ARTICLE

Reversing the Epithelial–Mesenchymal Transition in Metastatic Cancer Cells Using CD146-Targeted Black Phosphorus Nanosheets and a Mild Photothermal Treatment

Jinyuan Liu, Steve Smith, and Congzhou Wang*

Cite This: https://doi.org/10.1021/acsnano.1c11070

Read Online

ACCESS | Metrics & More | Article Recommendations | Supporting Information

ABSTRACT: Cancer metastasis leads to most deaths in cancer patients, and the epithelial–mesenchymal transition (EMT) is the key mechanism that endows the cancer cells with strong migratory and invasive abilities. Here, we present a nanomaterial-based approach to reverse the EMT in cancer cells by targeting an EMT inducer, CD146, using engineered black phosphorus nanosheets (BPNSs) and a mild photothermal treatment. We demonstrate this approach can convert highly metastatic, mesenchymal-type breast cancer cells to an epithelial phenotype (*i.e.*, reversing EMT), leading to a complete stoppage of cancer cell migration. By using advanced nanomechanical and super-resolution imaging, complemented by immunoblotting, we validate the phenotypic switch in the cancer cells, as evidenced by the altered actin organization and cell morphology, downregulation of mesenchymal protein markers, and upregulation of epithelial protein markers. We also elucidate the molecular mechanism behind the reversal of EMT. Our results reveal that CD146-targeted BPNSs and a mild photothermal treatment synergistically contribute to EMT reversal by downregulating membrane CD146 and perturbing its downstream EMT-related signaling pathways. Considering CD146 overexpression has been confirmed on the surface of a variety of metastatic, mesenchymal-like cancer cells, this approach could be applicable for treating various cancer metastasis *via* modulating the phenotype switch in cancer cells.

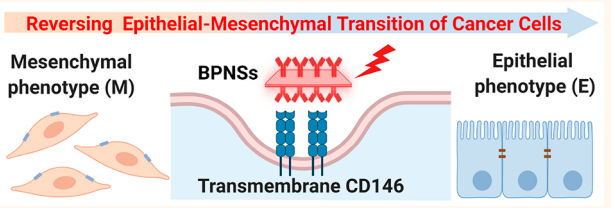

KEYWORDS: *epithelial–mesenchymal transition, phenotype modulation, cancer metastasis, CD146, black phosphorus nanosheets, mild photothermal treatment*

Cancer metastasis causes ~90% mortality in cancer patients, and the epithelial–mesenchymal transition (EMT) is the key mechanism for cancer metastasis.[1−3] During EMT, epithelial cancer cells evolve into a mesenchymal phenotype through the suppression of epithelial markers, upregulation of mesenchymal markers, and reorganization of actin cytoskeleton, which endow cancer cells with strong migratory and invasive capabilities.[4] EMT is also known to mediate the progression of drug resistance and contribute to cancer metastasis following chemotherapy.[5] Hence, emerging evidence suggests that targeting EMT can be a standalone therapeutic strategy or can improve the effectiveness of classic approaches for treating cancers.[6] However, translation of EMT targeted compounds to the clinic has been challenging due to the lack of molecular–cellular targeting specificity and efficacy.[7] Moreover, most of these compounds focus on the prevention of EMT rather than on the cancer cells that have already undergone EMT.[6] Therefore, approaches that are more specific, effective, and broadly applicable to eliminate mesenchymal-type cancer cells with high metastatic capability and enhanced drug resistance hold great promise to revolutionize the treatment of cancer metastasis.

Photothermal therapy (PTT) has been reported for treating cancer metastasis in the recent years, thanks to its non-invasiveness and excellent spatial–temporal selectivity.[8] This

Received: December 13, 2021
Accepted: January 20, 2022

Scheme 1. Concept of Reversing the Epithelial–Mesenchymal Transition (EMT) in Metastatic, Mesenchymal-Type Cancer Cells *via* Targeting a Transmembrane EMT Inducer, CD146, Using Engineered Black Phosphorus Nanosheets (BPNSs) and a Mild Photothermal Treatment (PTT)[a]

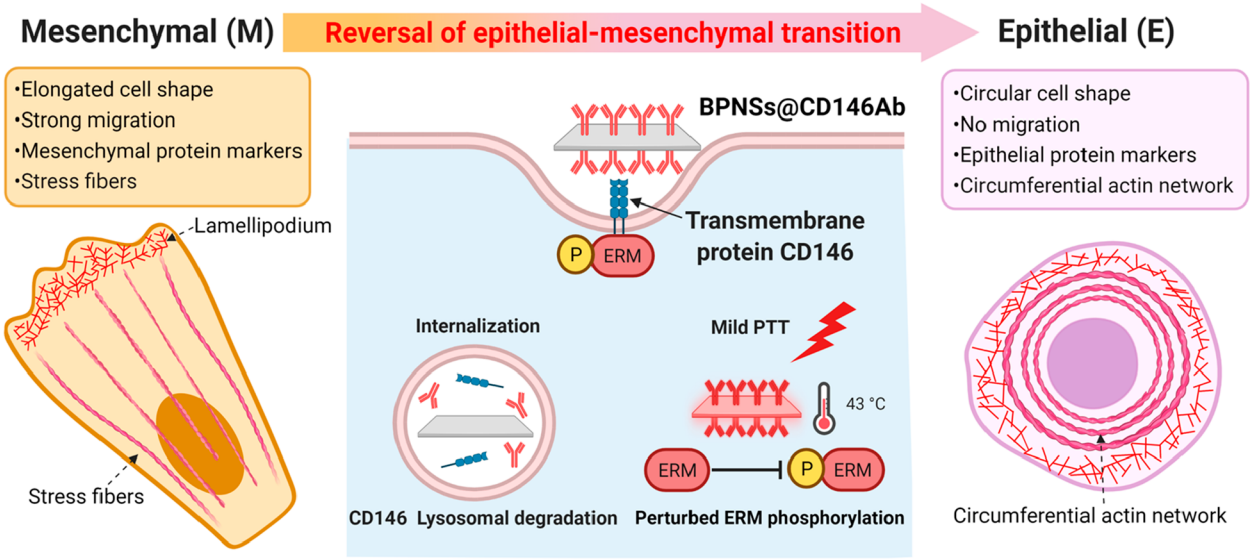

[a]CD146-targeted BPNSs (*i.e.*, BPNSs@CD146Ab) and a mild PTT are expected to synergistically contribute to the reversal of EMT by downregulating membrane CD146 and perturbing phosphorylation of ezrin/radixin/moesin (ERM).

strategy relies on loading photo-absorbers into the tumor and generating a local hyperthermia to thermally ablate cancer cells using near-infrared (NIR) laser irradiation.[9−13] So far, PTT has been used to directly ablate primary tumor and nearby metastatic sites, or in combination with other therapeutic approaches to treat metastatic cancer cells located at the distant organs.[8] However, implementing PTT in clinical settings still faces two main obstacles: First, since it is difficult to load photo-absorbers homogeneously in the tumor, especially in the tumor margins, which usually contain a large portion of metastatic cells, the temperatures in these regions are not adequate to eradicate all tumor cells, leaving behind viable tumor cells that can still migrate.[14] Second, an elevated local temperature (typically above 50 °C) is needed to thermally kill/ablate cancer cells,[15−17] which necessitates the use of high laser intensity that exceeds the safety limit (*i.e.*, the American National Standards Institute defines maximal permissible exposure to be 0.35 W/cm^2 for NIR lasers),[18] resulting in adverse effects on normal tissues such as skin damage and scar formation.[19] Based on these considerations, we are motivated to seek alternative strategies that can overcome the current problems associated with PTT for the treatment of cancer metastasis. A potential solution could be applying a mild photothermal effect (*i.e.*, 42−45 °C induced by a minimal dosage of photo-absorbers and low laser intensity) to stop cancer metastasis in cases where elevated temperatures (>50 °C) for thermal ablation cannot be achieved due to the above-stated reasons.

Cluster of differentiation 146 (CD146) was originally recognized to be a melanoma-specific cell adhesion molecule (MCAM).[20−22] In fact, a variety of cancers present overexpressed CD146 on their cell surface including breast, prostate, ovarian, and lung cancers, and high levels of surface CD146 are closely linked to metastasis propensity of these cancers and a poor prognosis.[23−26] It was found that CD146 acts as an EMT inducer *via* activation of a small GTPase protein (*i.e.*, RhoA), and the RhoA activation regulates reorganization of actin cytoskeleton and expression of EMT transcriptional factors, thereby triggering the EMT process and leading to metastasis of cancer cells.[27,28] Conversely, downregulation of CD146 drives the mesenchymal-type cells to lose their mesenchymal traits and recover their epithelial phenotype, leading to reduced cell migration and invasion.[27] Thus, CD146, as an EMT regulator, is a potential therapeutic target for treating metastasis for a number of cancers.

Here, we present a nanomaterial-based approach to reverse the EMT of cancer cells *via* targeting an EMT inducer, membrane CD146, using engineered black phosphorus nanosheets (BPNSs) and a mild photothermal treatment (Scheme 1). We use BPNSs in this approach as photo-absorbers because of their large surface-to-volume ratios, ease of surface functionalization, excellent biodegradability, and superior photothermal conversion efficiency compared to metal-based plasmonic nanomaterials.[29−31] Our central hypothesis is that CD146-targeted BPNSs and a mild photothermal treatment will synergistically contribute to the reversal of EMT in mesenchymal-type cancer cells and thus stop the migration of cancer cells. To demonstrate the feasibility of this approach, we select MDA-MB-231, a triple-negative, mesenchymal-type breast cancer cell line, as the testbed. We functionalize the BPNSs surface with CD146 antibodies, which serve a two-fold purpose: (1) to deliver nanosheets specifically into cancer cells and, more importantly, (2) to perturb the EMT inducer (*i.e.*, CD146) and its downstream EMT-related effectors, including the cell's phenotype and migration ability. Using advanced single-cell imaging techniques, as well as classic Western blotting and cell migration assays, we demonstrate that this approach can convert mesenchymal-type cancer cells to an epithelial phenotype, resulting in a complete stoppage of cell migration. In the end, we further elucidate the molecular mechanism of the reversal of EMT. To our knowledge, 2D materials to date have only been found to cause the EMT (*e.g.*, graphene oxide),[32] but not reverse the EMT, and photothermal

https://doi.org/10.1021/acsnano.1c11070
ACS Nano XXXX, XXX, XXX−XXX

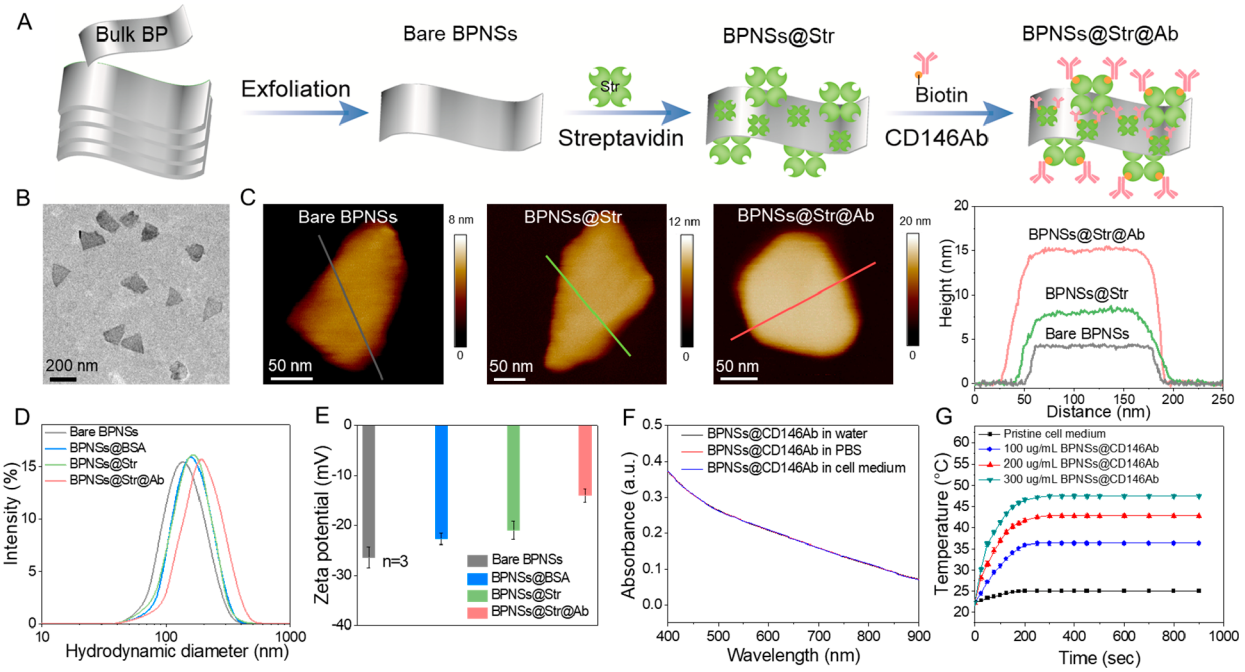

Figure 1. Characterization of CD146 antibody-functionalized BPNSs. (A) Workflow for functionalizing the surface of BPNSs with CD146 antibodies. The exfoliated BPNSs are first coated with a layer of streptavidin and then conjugated with biotin-labeled CD146 antibodies. (B) TEM image of the exfoliated BPNSs from bulk BP (prior to surface functionalization). (C) AFM characterization of surface functionalization of BPNSs. A progressive increase in nanosheet thickness can be observed following each step of functionalization. (D) Hydrodynamic diameter and (E) surface potential of BPNSs (measured in water) following the stepwise functionalization. The increased hydrodynamic diameter and surface potential suggest successful surface functionalization. (F) UV−vis absorbance spectra of BPNSs@CD146Ab in different liquid media. (G) Temperature profiles of pristine cell medium and cell media containing different concentrations of BPNSs@CD146Ab upon NIR laser irradiation (808 nm, 0.35 W/cm^2). Error bars in panels E and G are from three independent measurements (n = 3).

treatment so far has not been applied to modulate the EMT in cancer cells. Our approach clearly offers a nanomaterial-based strategy for treating cancer metastasis through modulating the epithelial/mesenchymal phenotype of cancer cells.

RESULTS AND DISCUSSION

Preparation of CD146 Antibody-Functionalized BPNSs. Figure 1A illustrates the procedure of functionalizing BPNSs with CD146 antibodies. The surface of BPNSs is coated with a layer of streptavidin and then conjugated with biotin-labeled CD146 antibodies. This surface functionalization strategy offers two advantages: (1) it prevents antibodies from directly contacting with the nanosheet surface, which may cause inactivation of antibodies,[33] and (2) it maximizes the surface coverage of CD146 antibodies, as each streptavidin contains multiple biotin binding pockets.[34]

First, BPNSs were obtained using a mechanical exfoliation method.[29,30,35] The bulk BP was sonicated for 12 h in a sodium hydroxide-saturated *N*-methyl-2-pyrrolidone solution, which provides superior exfoliation efficacy and prevents the oxidation and degradation of BP.[36] Transmission electron microscopy (TEM, Figure 1B) showed that the exfoliated BPNSs are free-standing, with a uniform lateral dimension of 158 ± 25 nm. Subsequently, the surface of BPNSs was coated by a streptavidin layer based on the strong protein-binding capacity of BPNSs,[37] followed by the conjugation of biotin-labeled CD146 antibodies. Atomic force microscopy (AFM) proved the surface functionalization of BPNSs in a stepwise manner. As shown in Figure 1C, the thickness of BPNSs elevated from ∼4 to ∼8 nm following coating with streptavidin (*i.e.*, from bare BPNSs to BPNSs@Str), and further increased to ∼15 nm after conjugating with biotin-labeled CD146 antibodies (*i.e.*, from BPNSs@Str to BPNs@Str@Ab). The increased thicknesses are reasonable, considering the smaller molecular size of streptavidin (4.2 × 4.2 × 5.6 nm) versus the larger molecular size of antibody (14.5 × 8.5 × 4 nm).[38] The coating of streptavidin was further determined to be a monolayer by the protein quantification assay (Supporting Information). Moreover, TEM imaging of the final product (*i.e.*, BPNSs@Str@Ab) revealed that the lateral dimension of the nanosheets increased to 167 ± 27 nm after the two-step surface functionalization (Figure S1). Apart from the topographic characterizations, dynamic light scattering (DLS) and zeta potential analyses also suggested successful surface functionalization, as manifested by the gradually increased hydrodynamic diameter and surface potential of the nanosheets (Figure 1D,E). As control, bovine serum albumin (BSA)-coated BPNSs (BPNSs@BSA) were prepared as non-targeted nanosheets. The excellent colloidal stability of BPNSs@Str@Ab in various media, including water, PBS, and cell culture medium (*i.e.*, DMEM + 10% serum), within 1 week was further validated using DLS, as their hydrodynamic diameter showed no obvious change (Figure S2). Figure 1F,G summarizes the optical and photothermal properties of BPNSs@Str@Ab (hereafter referred to as BPNSs@CD146Ab). The broad absorption spectrum of BPNSs@CD146Ab, spanning from the ultraviolet to the NIR region, makes it an ideal photothermal agent (Figure 1F).[39−41] Compared to bare BPNSs, surface functionalization with antibodies prevents the degradation of BPNSs@CD146Ab in the various media, as demonstrated by the strong absorption maintained after 1 week (Figure S3). Upon the irradiation of

https://doi.org/10.1021/acsnano.1c11070
ACS Nano XXXX, XXX, XXX−XXX

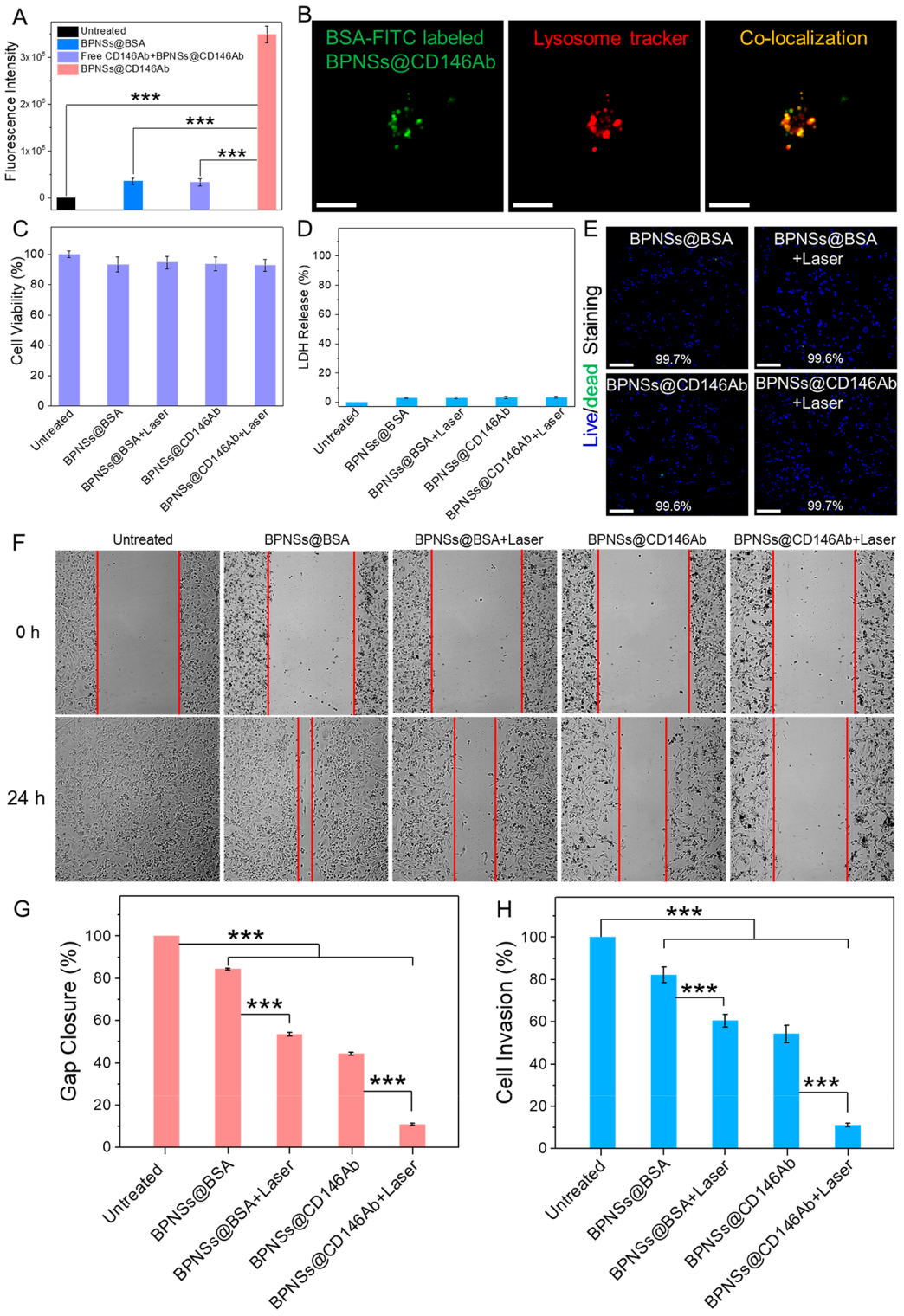

Figure 2. Cell uptake and cytotoxicity assessment of BPNSs, along with their effects on MDA-MB-231 cell migration. (A) Quantitative analysis of cell uptake amount of FITC-labeled BPNSs using correlated total cell fluorescence (CTCF) method. Error bars: $n = 10$ cells. One-way ANOVA, $^{***}P < 0.001$. (B) Sub-cellular localization of FITC-labeled BPNSs@CD146Ab. The overlapped green (from FITC) and red fluorescence (from lysosome probe) indicates the co-localization of BPNSs@CD146Ab with late endosomes/lysosomes. Scale bars: 10 μm. (C) MTT, (D) lactate dehydrogenase (LDH), and (E) live/dead staining assays demonstrating the negligible cytotoxicity of BPNSs and a follow-up laser treatment. Scale bars: 100 μm. LDH assay indicates the membrane integrity, as intracellular LDH can release to the cell medium upon membrane damage. Error bars: $n = 5$ assay wells. One-way ANOVA, $^{***}P < 0.001$. (F, G) 2D scratch assays evaluating the cell migration subjected to different treatment conditions. (H) 3D invasion assay assessing the migration of the cells subjected to the five treatment conditions. Error bars in panels G and H represent four independent experiments ($n = 4$). One-way ANOVA, $^{***}P < 0.001$. Both cell migration assays demonstrate BPNSs@CD146Ab with mild photothermal treatment can almost stop the cancer cell migration.

https://doi.org/10.1021/acsnano.1c11070
ACS Nano XXXX, XXX, XXX−XXX

an 808 nm laser (0.35 W/cm^2), cell growth medium with 200 μg/mL BPNSs@CD146Ab increased the temperature from 22.3 to 42.8 °C within 5 min, whereas the pristine cell medium had only a negligible temperature rise (Figure 1G). From the literature, this mild temperature rise (to ∼43 °C) should not kill the cancer cells.[14] The photothermal stability of BPNSs@CD146Ab was further verified by the unchanged temperature profile after repeated laser irradiation cycles and storage in cell culture medium for at least 1 week (Figure S4). Together, these results provide solid evidence indicating the successful preparation of CD146 antibody-functionalized BPNSs (*i.e.*, BPNSs@CD146Ab), along with excellent colloidal, material, and photothermal stability.

Cell Uptake and Cytotoxicity Assessment of CD146 Antibody-Functionalized BPNSs. We selected a triple-negative breast cancer cell line (*i.e.*, MDA-MB-231) as our cell model because of its high expression of surface CD146,[23,26,27] which was verified by immunofluorescence experiments (Figure S5). To track the cell uptake of BPNSs, BPNSs@CD146Ab and BPNSs@BSA (*i.e.*, the non-targeted control) were labeled with the same amount of FITC-BSA by fixing the molar ratio of streptavidin or BSA to FITC-BSA at 3:1 during the first coating step. These surface coatings were demonstrated to be stable in various media, including in water, slightly acidic PBS (pH = 6.4), and cell culture medium, since only a minimal amount of FITC-BSA was detected in the supernatants after 2 days of storage (Figure S6). The cells were cultured with FITC-labeled BPNSs@CD146Ab or BPNSs@BSA for 12 h. Fluorescence microscopy and quantitative analysis using a correlated-total-cell-fluorescence approach[42] showed higher uptake of BPNSs@CD146Ab by the cells, suggesting that CD146 antibodies functionalized on the surface of BPNSs facilitated their cellular internalization (Figure 2A and Figure S7). This was further substantiated by a receptor blocking experiment, wherein a drastic decrease in the cell uptake of BPNSs@CD146Ab can be observed if the cells were pre-treated with free CD146 antibodies. The subcellular localization of BPNSs@CD146Ab was studied by a fluorescent probe for late endosome/lysosome staining, namely, Lysotracker Red.[43] As shown in Figure 2B and Figure S8, the fluorescence from FITC-labeled BPNSs@CD146Ab (shown as green color) overlapped with the fluorescence of the lysosome probe (shown as red color), indicating that the internalized BPNSs@CD146Ab were located in late endosomes/lysosomes.[44] The cytotoxicity of BPNSs@CD146Ab and BPNSs@BSA (12 h incubation with cells), with or without a follow-up laser irradiation (0.35 W/cm^2, 5 min), was evaluated by performing a suite of cytotoxicity assays, including a viability assay and two assays indicating the integrity of plasma membrane (Figure 2C−E and Figure S9). These assays demonstrate the cancer cells had almost no damage in cell viability and plasma membrane in all experimental groups, suggesting that these treatments did not kill the cancer cells or affect their viability. Hence, these mild treatments were applied in the subsequent studies for investigating their effects on the motility and phenotype of the cancer cells.

BPNSs@CD146Ab with Mild Photothermal Treatment Stops Cancer Cell Migration. Next, we aimed to evaluate the impact of these treatments on the cancer cell motility. The mesenchymal-type cancer cells, including MDA-MB-231 cells, are recognized to possess strong migratory and invasive abilities, and overexpression of cell surface CD146 is directly connected to the increased probability of cancer metastasis, leading to high mortality in cancer patients.[23,27,45] A scratch assay (2D) and an invasion assay (3D) were conducted to quantify the MDA-MB-231 cell migration subjected to different treatment conditions, including cells without treatment, cells treated by BPNSs@BSA, cells treated by BPNSs@BSA plus laser, cells treated by BPNSs@CD146Ab, and cells treated by BPNSs@CD146Ab plus laser. In the scratch assay, a small gap was created on the monolayer of cells by scratching the cell dish using a pipet tip, and cell migration was calculated by the % of gap closure within a given period of time (*i.e.*, 24 h).[46,47] As shown in Figure 2F,G, the cells without treatment completely closed the gap within 24 h, owing to the strong migration nature of MDA-MB-231 cells. The cells treated by BPNSs@BSA showed a slightly decreased migration (*i.e.*, 84.4% gap closure within 24 h), and the BPNSs@BSA plus laser treatment further attenuated the cell migration (*i.e.*, 53.5% gap closure within 24 h). Importantly, the cells treated with BPNSs@CD146Ab alone exhibited 44.3% gap closure, while the introduction of a follow-up laser treatment nearly stopped the cell migration, as evidenced by only 10.9% gap closure within 24 h. As control experiments, a stand-alone laser or heat treatment (*i.e.*, leaving cells in 43 °C incubator for 30 min) cannot slow down the cell migration, similar to cells without treatment (Figures S10 and S11). In the 3D assay, a trans-well insert was coated with Matrigel to mimic the extracellular matrix *in vivo*, and the cell invasion ability was determined by counting the cells that moved across the Matrigel matrix and adhered to the insert bottom.[48] As shown in Figure 2H, the lowest invasion can be observed on the cells treated with BPNSs@CD146Ab plus laser. In this case, only 10% of the cells invaded across the matrix within 24 h, compared to 100% invasion of cells without any treatment. The complete data sets of both cell migration assays in each experimental group are presented in Figures S12−S17. Overall, the consistent results from 2D and 3D assays demonstrate that BPNSs@CD146Ab with a mild laser treatment can almost halt the MDA-MB-231 cell migration. These results are outstanding, considering earlier reports based on other nanomaterials, such as metal nanoparticles, which can only hamper cancer cell migration to a lesser degree.[14,49−51] Here, the superb inhibition of cancer cell migration can be attributed to the synergistic effect of cell uptake of BPNSs@CD146Ab and a mild photothermal treatment.

BPNSs@CD146Ab with Mild Photothermal Treatment Alters Actin Cytoskeleton. Since we observed inhibited cancer cell migration, especially for the cells treated with BPNSs@CD146Ab plus laser, we began to look into the actin cytoskeleton, the "bone" structure of cancer cells that drives the cell's motility.[52−54] A live-cell imaging technique, nanomechanical AFM, was utilized to image the untreated and BPNSs@CD146Ab plus laser-treated cancer cells. The nanomechanical imaging here simultaneously collects cell morphology, surface topography, and elastic modulus images.[55−57] In particular, the elastic modulus image is well suited to resolve the dorsal stress fibers underlying the cell membrane, as these actin filaments make a primary contribution to the cellular stiffness (Figure 3A), as demonstrated by our previous work.[42] Considering the cells were probed with a spherical AFM tip, a Hertz model was applied to fit a total of 256 × 256 indentation curves collected on the imaging area (Figure 3B,C), and the acquired modulus values (in kilopascal, kPa) associated with specific (*X*, *Y*) coordinates were used to render the entire modulus image. Figure 3D shows the representative images of

https://doi.org/10.1021/acsnano.1c11070
ACS Nano XXXX, XXX, XXX−XXX

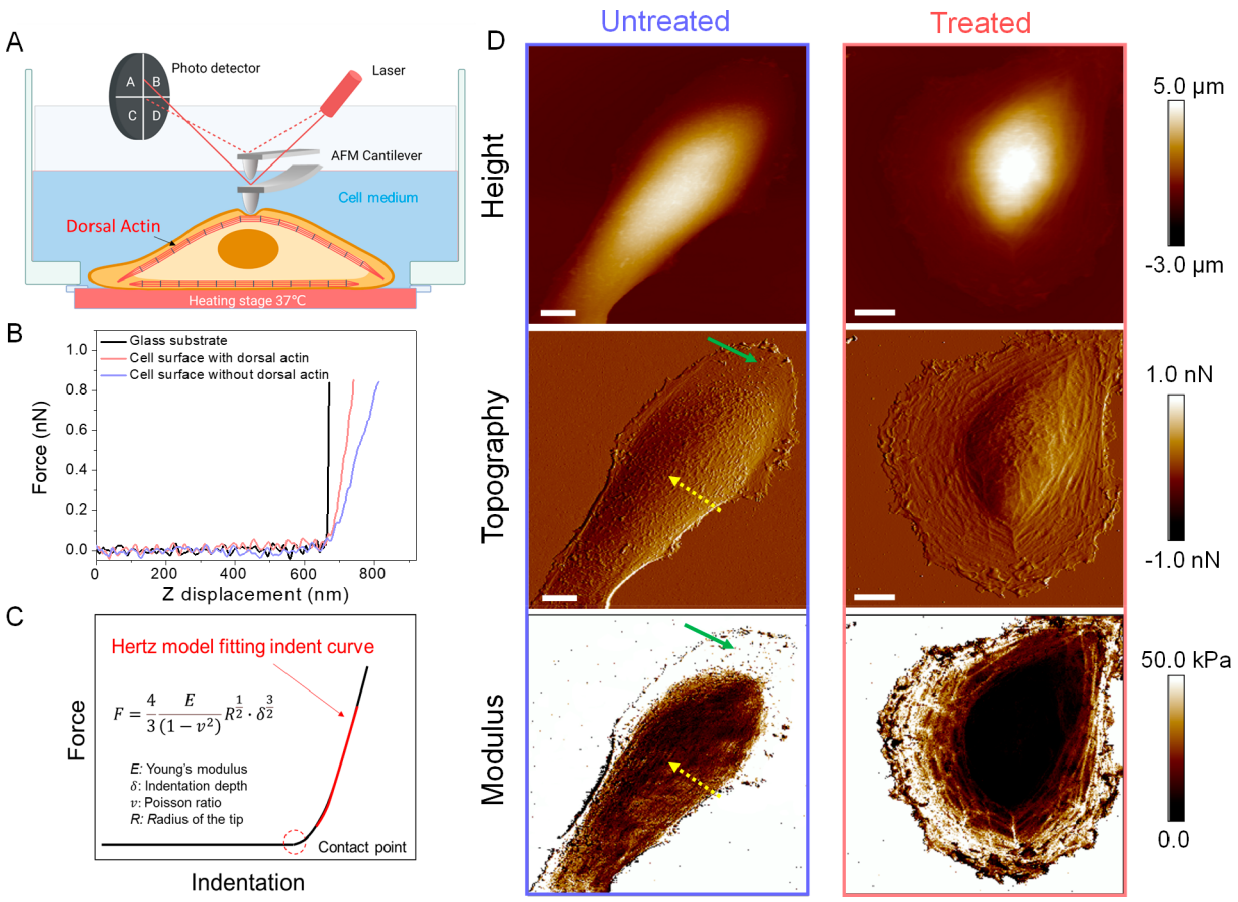

Figure 3. Nanomechanical characterization of single MDA-MB-231 cells, including untreated cells and cells treated with BPNSs@CD146Ab plus laser. (A) Schematic illustrating the setup for imaging dorsal actin underlying the surface of a live cell. (B) Representative indent curves obtained on different imaging areas such as on a glass substrate and on the cell top with or without underneath dorsal stress fibers. (C) Hertz model used to fit indent curves for calculation of elastic (Young's) modulus. (D) Representative images of untreated and treated MDA-MB-231 cells in height, topography, and modulus channels. In the untreated cell, the yellow arrows point to the dorsal stress fibers and the green arrows indicate the lamellipodia. The treated cell displays drastic changes in cell morphology and dorsal actin structure. Scale bar: 10 μm.

single cells in height, topography, and modulus channels. The complete AFM data sets for untreated and treated cells are displayed in Figures S18 and S19. It is noticeable that the cancer cells displayed a morphological change (*i.e.*, from an elongated to a circular shape) after the BPNSs@CD146Ab plus laser treatment, resulting in a reduced aspect ratio of single cells from 3.0 to 1.2 (Figure S20). In the untreated cells, two actin-related features that are typically found in mesenchymal-type cells can be discerned:[58] (1) dorsal stress fibers along the cell's long axis, marked by yellow arrows, explicitly correlated in modulus and topography channels, and (2) lamellipodia, the leading edge of motile cells, marked by green arrows, exhibiting higher modulus compared with other areas of the cell surface, due to the underneath actin network and a substrate effect.[59] In stark contrast, the treated cells not only lost the dorsal stress fibers but also appeared to develop a flat and thin membrane around the cell periphery with an underlying circumferential actin network. Herein, the disappearance of dorsal stress fibers also led to a lower average modulus on the treated cells (5 kPa, compared to 46 kPa for untreated cells), according to a statistical analysis of the elastic modulus on five cells (Figure S21).

We next examined the actin organization within the cell's ventral region using a super-resolution tool, direct stochastic optical reconstruction microscopy (dSTORM). Unlike conventional wide-field microscopy, dSTORM adopts total internal reflection illumination, which only excites a 100 nm thin layer above the coverslip and eliminates the background fluorescence outside the excitation field (Figure 4A). The working principle of dSTORM is depicted in Figure 4B,C: sparsely activate individual fluorophores, determine the positions of the fluorophores with sub-diffraction-limit precision, repeat this process for thousands of cycles, and reconstruct the high-resolution image by stacking the individual imaging frames.[60−62] The dSTORM imaging offers a drastically improved spatial resolution, which allows for precise quantification of ventral stress fibers (Figure 4D). More dSTORM images of cells with or without the treatment are included in Figures S22 and S23. Consistent with AFM imaging, the untreated cells possessed lamellipodia, the network of actin at the leading edge of the cells initiating the cell's movement, as well as ventral stress fibers spanning the cell's elongated body providing the contraction for the cell's movement. On the contrary, almost no ventral stress fibers can be found in treated cells (Figure S24), whereas a circumferential actin network developed around the cell periphery. Together, these imaging techniques demonstrate that CD146 antibody-functionalized BPNSs with mild photothermal effect altered the actin organization and cell morphology of MDA-MB-231 cells. The loss of lamellipodia and dorsal/ventral

https://doi.org/10.1021/acsnano.1c11070
ACS Nano XXXX, XXX, XXX−XXX

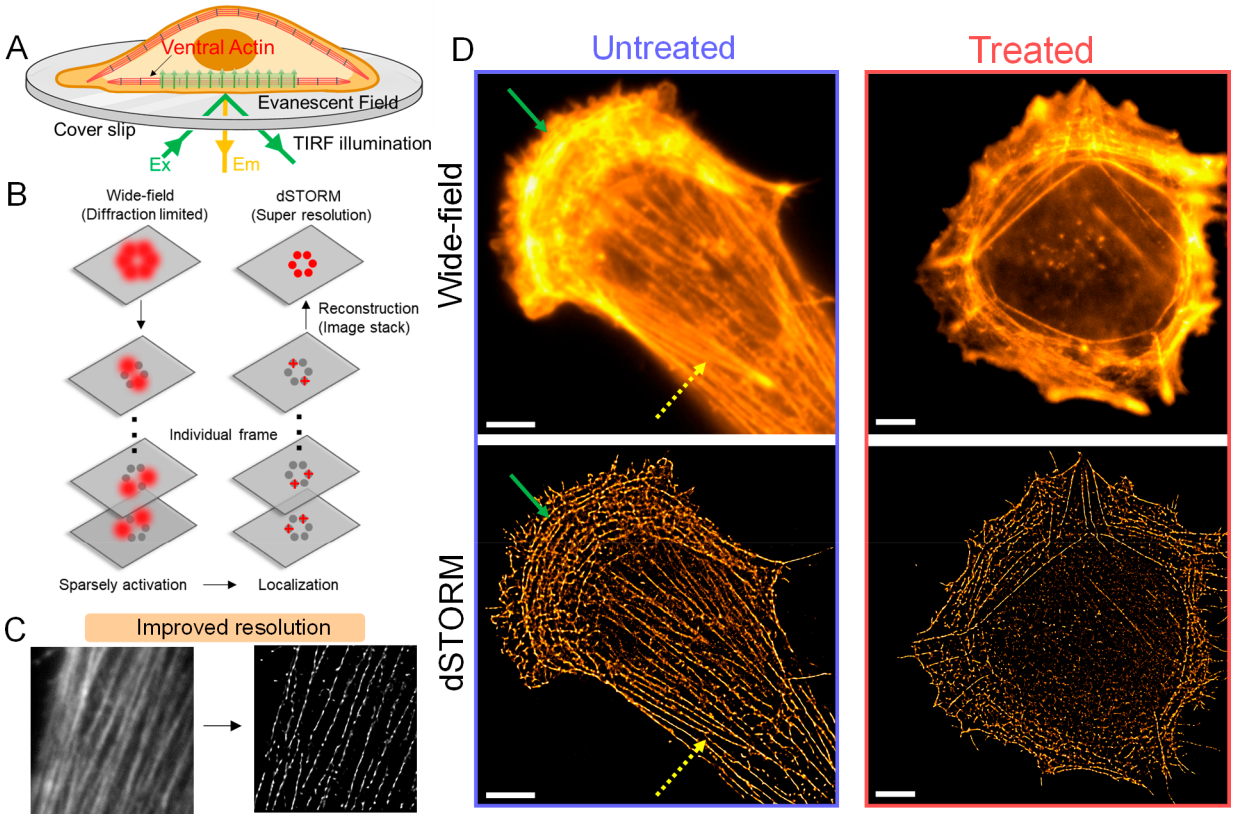

Figure 4. dSTORM imaging of actin organization at the ventral region of untreated and BPNSs@CD146Ab plus laser-treated MDA-MB-231 cells. (A) Diagram showing the application of the TIRF mode for imaging ventral actin. (B, C) Workflow of dSTORM: sparsely activate single fluorophores, determine their positions in individual frames, repeat this process for thousands of cycles, and reconstruct the high-resolution image. (D) Wide-field and dSTORM images of ventral actin organization in untreated and treated cells. In the untreated cell, the yellow arrows indicate the ventral stress fibers, and the green arrows mark the lamellipodia. The treated cell exhibits the formation of a circumferential actin network and the loss of ventral stress fibers. Scale bar: 5 μm.

stress fibers (*i.e.*, two traits distinctive of mesenchymal-type cells)[63,64] and the appearance of a circumferential actin network (*i.e.*, a typical epithelial feature)[65,66] imply the phenotypic switch of the cancer cells from a mesenchymal to an epithelial state. Interestingly, we also observed a similar phenomenon on a melanoma cell line (*i.e.*, CD146-positive SKMEL2),[67] where the cells reorganized the actin structure and stopped their migration after treatment by BPNSs@CD146Ab plus laser (Figure S25). This suggests the applicability of this approach in treating different cancers with overexpressed cell surface CD146.

BPNSs@CD146Ab with Mild Photothermal Treatment Reverses the EMT. Following the imaging characterization of single cells, we turned our attention to the epithelial and mesenchymal protein markers in the cancer cells. Previous studies suggest that the cytoskeletal and morphological changes during EMT in cancer cells are accompanied by suppression of epithelial proteins and gain of mesenchymal proteins.[7] Among others, the cadherin switch from E-cadherin to N-cadherin represents the hallmark of EMT, during which cells lose their stable cell-to-cell contacts while acquiring a mesenchymal phenotype with enhanced migration tendency (Figure 5A).[68] Hence, to further substantiate the phenotypic effect of BPNSs@CD146Ab and mild photothermal treatment on MDA-MB-231 cells, Western blots were conducted to quantify two classic mesenchymal proteins (N-cadherin and vimentin, Figure 5B,C) and two epithelial proteins (E-cadherin and cytokeratin, Figure 5D,E) in the cells. As expected, the untreated cells possessed dominant levels of N-cadherin and vimentin, along with low amounts of their epithelial counterparts, E-cadherin and cytokeratin, indicating a mesenchymal nature of MDA-MB-231 cells. For the cells treated by BPNSs@CD146Ab alone, both N-cadherin and vimentin showed a 40−50% decrease in expression levels, whereas the expression of E-cadherin and cytokeratin nearly doubled. More importantly, the cells treated with BPNSs@CD146Ab plus laser further reduced the expression of N-cadherin and vimentin (70−80% decrease, relative to untreated cells) and concurrently increased the levels of E-cadherin and cytokeratin (a 4−5-fold increase relative to untreated cells). Together, these results demonstrate that BPNSs@CD146Ab with mild photothermal treatment synergistically downregulated mesenchymal proteins and upregulated epithelial proteins in MDA-MB-231 cells, which further ascertained the phenotypic switch from a mesenchymal to an epithelial phenotype (*i.e.*, the reversal of EMT) in these cancer cells.

Molecular Mechanism of EMT Reversal Induced by BPNSs@CD146Ab with Mild Photothermal Treatment. Finally, we sought to understand the mechanism of how BPNSs@CD146Ab with mild photothermal treatment reversed the EMT in the mesenchymal-type MDA-MB-231 cells. Prior studies suggested that transmembrane CD146 induces the EMT *via* activation of RhoA, a small GTPase that upregulates stress fiber formation, and EMT-inducing transcriptional factors which inhibit E-cadherin transcription, thereby endowing cancer cells with a mesenchymal phenotype

https://doi.org/10.1021/acsnano.1c11070
ACS Nano XXXX, XXX, XXX−XXX

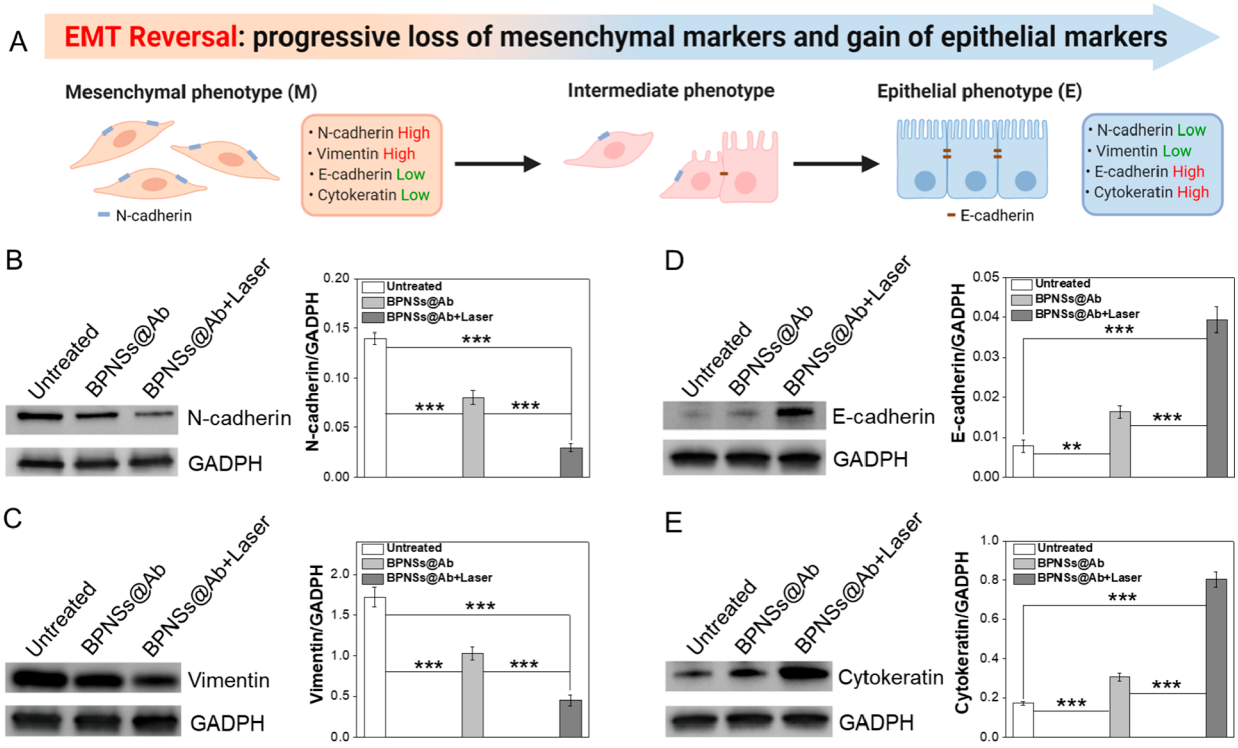

Figure 5. (A) Schematic summarizing the changes of protein markers during the reversal of the EMT process. (B, C) Western blotting analysis of the mesenchymal proteins (N-cadherin and vimentin) in MDA-MB-231 cells after different treatments, including cells without treatment, cells treated with BPNSs@CD146Ab alone, and cells treated with BPNSs@CD146Ab plus laser. (D, E) Western blotting analysis of the epithelial proteins (E-cadherin and cytokeratin) in the cells after the different treatments. GADPH serves as a housekeeping protein. Error bars: $n = 3$. One-way ANOVA, $^{**}P < 0.01$, $^{***}P < 0.001$.

with strong migration ability.[27,69] Figure 6A (left column) illustrates the molecular mechanism of CD146-regulated RhoA activation: The transmembrane CD146 recruits Rho-guanine-nucleotide dissociation inhibitory factors α (RhoGDIα, a RhoA inhibitor) through the phosphorylated ezrin/radixin/moesin (p-ERM) and thus releases RhoA-GDP from its inhibitory interaction with RhoGDIα, which facilitates subsequent RhoA activation to RhoA-GTP.[69,70] Herein, both CD146 and p-ERM play indispensable roles in the RhoA activation because both of them are necessary for recruiting RhoGDIα, *i.e.*, sequestering the RhoA inhibitor from RhoA-GDP and thereby releasing RhoA-GDP for subsequent activation.[22] Inspired by these findings, we hypothesized that CD146-targeted BPNSs@CD146Ab and mild photothermal treatment will synergistically contribute to the reversal of EMT by depleting membrane CD146 (Figure 6A, middle column) and interrupting ERM phosphorylation (Figure 6A, right column), where both factors will hinder the sequestration of the RhoA inhibitor and, in turn, downregulate RhoA activation and its downstream EMT-related effectors, leading to the reversal of EMT.

To test our hypothesis, membrane CD146 was first quantified by Western blots. Figure 6B shows that cells treated by BPNSs@CD146Ab alone and cells treated by BPNSs@CD146Ab plus laser, in both cases, displayed a ~40% drop in the membrane CD146, compared to untreated cells. This is because the endocytosis of BPNSs@CD146Ab directed the membrane CD146 to a lysosomal-degradation pathway, as validated by the earlier sub-cellular localization analysis. Given the critical role of CD146 in the induction of EMT, these results justify our earlier observations from EMT protein markers and cell motility, wherein BPNs@CD146Ab treatment alone can moderately reverse the EMT. Indeed, these results are aligned with earlier literature revealing that downregulating surface CD146 in mesenchymal-type breast cancer cells can partially reverse their phenotype.[23,27] Thus, it is rational to conclude that the endocytosis of BPNSs@CD146Ab downregulates the CD146 on the cell membrane and decreases the anchoring sites on the cell membrane for sequestering RhoGDIα (*i.e.*, the RhoA inhibitor) from RhoA, as schematically illustrated in Figure 6A (middle column). Next, to gain insight into the effect of mild photothermal treatment on the reversed EMT, we focused on the ERM phosphorylation, another required factor for sequestering RhoGDIα from RhoA and preventing its inhibitory association with RhoA. The p-ERM and total-ERM levels within the cytoplasm were quantified by Western blots (Figure 6C). After treatment with BPNSs@CD146Ab alone, the cells had a reduction in ERM phosphorylation, as manifested by a half-declined p-ERM to total ERM ratio. Interestingly, this decrease in ERM phosphorylation corresponds with the downregulated membrane CD146 (~40% as noted above). This is as expected since a previous work found that transmembrane CD146 governs the phosphorylation of cytoplasmic ERM complex and their levels can be precisely correlated with each other.[22] Significantly, for the cells treated with BPNSs@CD146Ab plus laser, the ratio of p-ERM to total ERM exhibited an even larger decrease (~80%). Following the cell uptake of BPNSs@CD146Ab, the laser treatment induces a heat stress within the cell, which perturbs the phosphorylation of the ERM complex

https://doi.org/10.1021/acsnano.1c11070
ACS Nano XXXX, XXX, XXX−XXX

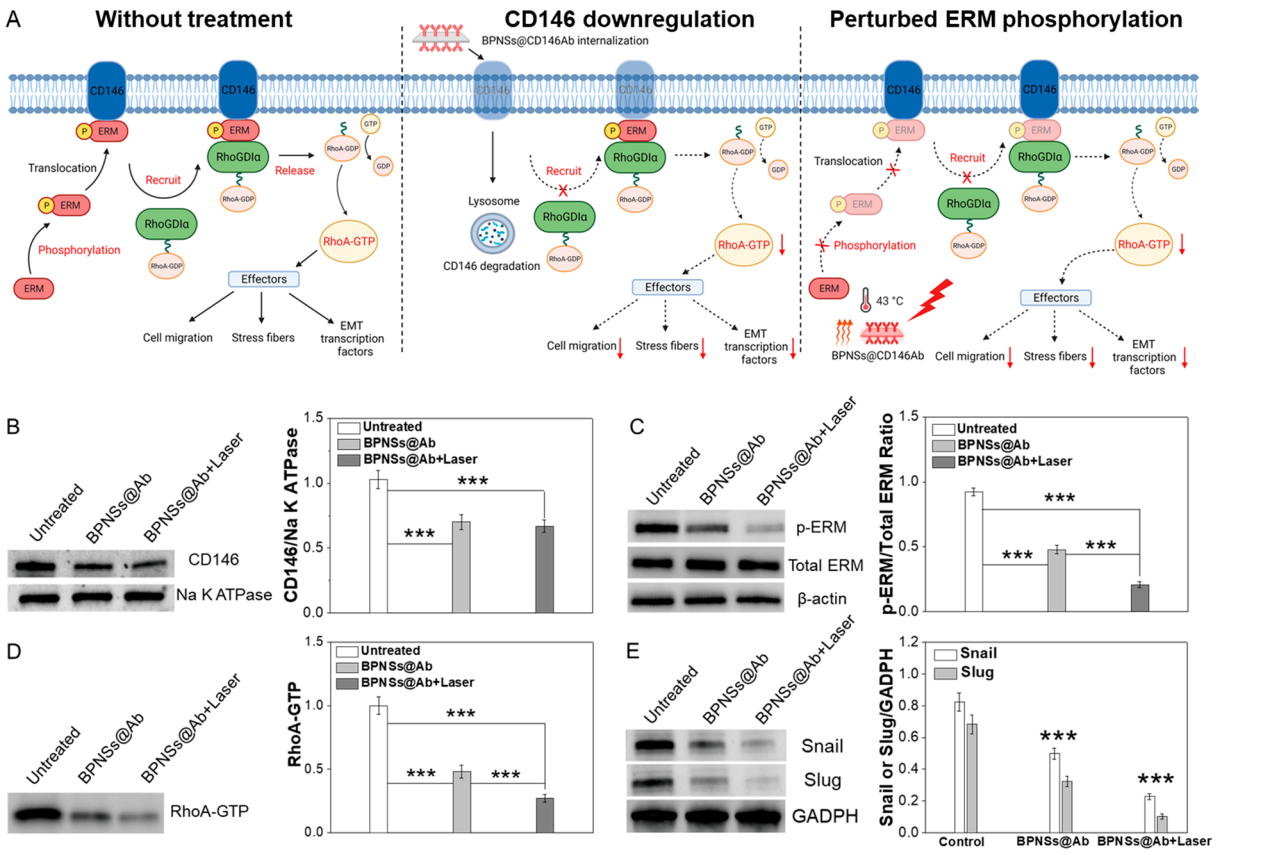

Figure 6. Molecular mechanism of EMT reversal induced by BPNSs@CD146Ab and laser treatment. (A) Left column: Molecular mechanism of CD146-regulated RhoA activation in untreated cells. Middle column: Endocytosis of BPNSs@CD146Ab downregulates the membrane CD146 *via* directing transmembrane CD146 to a lysosomal degradation pathway. Right column: Intracellular heat stress induced by laser irradiation perturbs ERM phosphorylation. Both factors hamper the sequestration of RhoGDIα (*i.e.*, the RhoA inhibitor) from RhoA and downregulate RhoA activation as well as its downstream effectors, including stress fiber formation, cell migration, and EMT protein transcription, thus inverting the mesenchymal-type cancer cells to an epithelial phenotype. (B–E) Western blot analyses of (B) membrane CD146, (C) p-ERM to total ERM ratio, (D) RhoA-GTP, and (E) EMT transcriptional factors (Snail and Slug) in MDA-MB-231 cells subjected to different treatments. Na K ATPase serves as a housekeeping protein of the membrane. β-Actin and GADPH serve as cytoplasmic housekeeping proteins. Error bars: $n = 3$. One-way ANOVA, $^{***}P < 0.001$.

and further reduces the required "crosslinkers" (*i.e.*, p-ERM) that recruit the RhoGDIα to the remaining transmembrane CD146, as schematically illustrated in Figure 6A (right column). Consistently, previous studies also reported that the heat stress can impair the intracellular protein phosphorylation in different types of cells.[14,71,72] Together, both cell uptake of BPNSs@CD146Ab and a follow-up laser treatment hindered the sequestration of RhoGDIα (the RhoA inhibitor) from RhoA, thus blocking the subsequent pathway for RhoA activation.

With a clear understanding of how the treatments affected the upstream pathway of RhoA activation, we next measured the activation level of RhoA by measuring RhoA-GTP (Figure 6D), an active form of RhoA in the cytoplasm, as well as its downstream EMT-inducing transcriptional factors including Snail and Slug, both of which proved to repress E-cadherin transcription and promote N-cadherin transcription.[73,74] Previous studies reported that the downregulation of RhoA and its downstream EMT transcriptional factors both can restore the epithelial phenotype of cancer cells.[75,76] Consistent with the observations on membrane CD146 and cytoplasmic p-ERM levels, cells treated with BPNSs@CD146Ab alone showed a ∼40–50% decrease in RhoA-GTP, whereas the introduction of laser irradiation further downregulated the RhoA-GTP by ∼70–80%. As expected, the downstream EMT-inducing transcriptional factors, Snail and Slug, also exhibited similar decreasing trends (Figure 6E), which can be correlated with the decreased levels of RhoA-GTP. Taken together, these molecular-level studies unravel the EMT-reversing mechanism: (1) cell uptake of BPNSs@CD146Ab downregulates the transmembrane CD146, thus reducing the membrane sites for sequestering RhoGDIα from RhoA, and (2) following the cell uptake of BPNs@CD146Ab, a mild hyperthermia upon a NIR laser irradiation interrupts the ERM phosphorylation, thus further reducing the "bridges" that link RhoGDIα to the remaining transmembrane CD146. Both factors hamper the sequestration of RhoGDIα (*i.e.*, the RhoA inhibitor) from RhoA and downregulate RhoA activation, as well as its downstream effectors, including stress fiber formation, cell migration, and EMT protein transcription, thus inverting the mesenchymal-type cancer cells to an epithelial phenotype.

CONCLUSION

We demonstrate that targeting a transmembrane EMT inducer, CD146, using BPNSs and a mild photothermal treatment can convert metastatic, mesenchymal-type breast cancer cells to an epithelial phenotype (*i.e.*, reversing EMT), leading to a complete stoppage of cancer cell migration. The phenotypic

https://doi.org/10.1021/acsnano.1c11070
ACS Nano XXXX, XXX, XXX–XXX

switch of MDA-MB-231 breast cancer cells involves altered actin organization and cell morphology, downregulation of mesenchymal protein markers, and upregulation of epithelial protein markers, as systematically investigated by advanced nanomechanical and super-resolution imaging and Western blot analysis. We also unveil the molecular mechanism behind the reversal of EMT. Our results reveal that CD146-targeted BPNSs with a mild photothermal treatment synergistically contribute to reverse EMT by depleting the membrane CD146 and perturbing ERM phosphorylation, where both factors downregulate RhoA activation and its downstream effectors, including stress fiber formation and EMT transcriptional factors, thereby inverting the mesenchymal-type cancer cells to an epithelial phenotype.

Overall, we have shown that (i) 2D materials (*i.e.*, BPNSs), with an appropriate design, can reverse the EMT in cancer cells, in contrast to inducing the EMT as recently reported for graphene oxide,[32] and (ii) the mild photothermal treatment here is used to modulate the phenotype of cancer cells, which deviates from the majority of earlier studies on photothermal therapy which applied elevated temperatures to ablate/kill cancer cells.[77−80] Considering CD146 overexpression is also confirmed on the surface of metastatic ovarian, prostate, melanoma, and lung cancer cells, this approach is expected to reduce progression and metastasis in a variety of cancers. Beyond this work, the reversal of EMT is also found to be a potent strategy to sensitize cancer cells to classical chemotherapeutics.[81,82] Therefore, we envision this approach holds tremendous potential *in vivo* in complementing current cancer treatments including surgical resection and chemotherapy to prevent cancer metastasis. For instance, following the surgical resection, this approach (*i.e.*, the combination of CD146-targeted BPNSs and mild PTT treatments) can be applied locally to constrain the migration of cancer cells remained in the tumor margin and sensitize these cancer cells to the classical anti-cancer drugs, thereby improving the success rate of surgical resection and chemotherapy, as well as the patient's prognosis.

EXPERIMENTAL SECTION

Preparation and Surface Functionalization of BPNSs. Five milligrams of BP powder (ACS Material, 7723-14-0) was added into a 10 mL sodium hydroxide-saturated *N*-methyl-2-pyrrolidone (Sigma-Aldrich, 328634) solution and sonicated in a glass tube for 12 h using an ultrasonic probe (power, 150 W; amplifier, 80%; on/off cycle, 45 s/15 s). The glass tube was maintained within ice−water during ultrasonication. After ultrasonication, the solution was subjected to a 10 000 rpm centrifugation for 10 min to separate the unexfoliated bulk BP. Next, the exfoliated BPNSs with 100−200 nm size can be collected by a 15 000 rpm centrifugation for 15 min. For preparing BPNSs@Str, BPNSs were added into a 2 mg/mL streptavidin (Leinco Technologies, S203) solution in water and left under bath sonication for 1 h, and then washed three times in distilled water using 15 000 rpm centrifugation (10 min for each time). The resulting BPNSs@Str were collected and re-dispersed in water for future use. The protocol for preparing BPNSs@BSA was similar as that of BPNSs@Str. For preparing BPNSs@Str@CD146Ab, the BPNSs@Str were placed in 50 μg/mL biotin-labeled CD146 antibody (R&D system, BAF932) in PBS for 1 h and then washed three times in PBS using 15 000 rpm centrifugation (10 min for each time).

Characterization of BPNSs. JEOL JEM 2100 LaB_6 TEM (200 keV) was used to collect TEM images of pristine and surface-functionalized BPNSs. Bruker BioScope Resolve AFM in a ScanAsyst mode was used to image pristine and surface-functionalized BPNSs in air. Bruker ScanAsyst Air HR probes with a tip radius of 2 nm were utilized for the AFM imaging. A Zetasizer Nano ZS system (Malvern Instruments) was applied for the hydrodynamic size and zeta potential measurements of BPNSs in different liquid media, including water, PBS, and cell culture medium. A Shimadzu-1900 spectrophotometer was utilized to collect absorbance spectra of BPNSs in the different liquid media.

Cytotoxicity Assays. Breast cancer or melanoma cells (MDA-MB-231 cell line from ATCC, HTB-26; SKMEL2 cell line from ATCC, HTB-68) were cultivated in DMEM/F12 cell medium (Gibco, 11320033) supplied with 10% fetal bovine serum (Gibco, 10082147). Three cytotoxicity assays (MTT cell viability assay from Thermo Fisher, V13154; LDH membrane integrity assay from Thermo Fisher, C20301; and live/dead staining assays from Thermo Fisher, R37609) were performed to assess the cytotoxicity of BPNSs and the mild photothermal treatment on the cells. The cells were seeded in a 96-well plate (8000−10 000 cells in each well) with 100 μL of cell medium. After culturing overnight, the old medium was replaced by a fresh medium added with 200 μg/mL BPNSs@CD146Ab or BPNSs@BSA. The cells were incubated with the BPNSs for another 12 h and then further treated with an 808 nm laser (0.35 W/cm^2, 5 min) on each well. The laser power density was calculated by 2 W of laser power divided by 2.7 cm diameter of laser spot size. The laser treatment was performed to cells without removing non-endocytosed BPNSs to ensure the consistency of the temperature rise of the cell medium (43 °C) across different wells. The cancer cells were subjected to five different treatment conditions, including untreated cells, cells treated by BPNSs@BSA, cells treated by BPNSs@BSA plus laser, cells treated by BPNSs@CD146Ab, and cells treated by BPNSs@CD146Ab plus laser. Each experimental condition contains quintuplicate wells.

Immunostaining of Cell Surface CD146. The protocol for immunostaining of cell surface CD146 on the cells followed the manufacturer's instruction for CD146 fluorescein-conjugated antibody (R&D System, FAB932F).

Cellular Internalization and Intracellular Localization of BPNSs. To track the internalization of BPNSs by cells, BPNSs@CD146Ab or BPNSs@BSA was labeled with a same amount of BSA-FITC (Thermo Fisher, A23015). During the first coating step, streptavidin or BSA was mixed with BSA-FITC at a 3:1 molar ratio. A total of 100 000 cells were seeded into a glass-bottom Petri dish (50 mm) and subsequently cultured with 200 μg/mL FITC-labeled BPNSs@CD146Ab or BPNSs@BSA for 12 h. In the receptor blocking assay, the cells were pre-treated using cell medium containing free CD146 antibodies (10 μg/mL) for 30 min, followed by incubating with 200 μg/mL FITC-labeled BPNSs@CD146Ab for 12 h. LysoTracker Red (Thermo Fisher, L7528) was used to label late endosomes/lysosomes. An Olympus fluorescence microscope (IX73) was used for fluorescence imaging. ImageJ software was used for quantifying cellular uptake of FITC-labeled BPNSs and sub-cellular localization analysis.

Cell Migration Assays. For the scratch assay, the cells were seeded into a 12-well plate (300 000 cells per well) to obtain a confluent monolayer. Next, 1 mL of fresh cell medium with 200 μg/mL BPNSs@CD146Ab or BPNSs@BSA was placed into each well and incubated for another 12 h, and then each well was irradiated by the NIR laser for 5 min. A pipet tip was applied for scratching a gap on the cell monolayer. The gap area was photographed instantly after scratching (0 h) and at the 24 h time point thereafter, and cell migration was calculated by the average percentage of gap closure. For the 3D invasion assay, a 12-well plate was seeded with MDA-MB-231 cells and then cultured with a medium with 200 μg/mL BPNSs@CD146Ab or BPNSs@BSA for another 12 h, followed by a 5 min laser treatment. Next, the treated cells were lifted and resuspended in a cell medium with 2% Matrigel (Corning). The above cell suspension was transferred to a 6.5 mm insert (pore size: 8 μm) precoated with Matrigel. Next, 1 mL of cell medium with 10% FBS was added to each well, and the invaded cells (*i.e.*, cells migrating through the pore and adhering to the bottom of insert) were stained and quantified after 24 h.

https://doi.org/10.1021/acsnano.1c11070
ACS Nano XXXX, XXX, XXX−XXX

AFM Imaging. A Bruker BioScope Resolve AFM in a quantitative nanomechanical imaging mode was applied to image untreated and BPNSs@CD146Ab + laser-treated cancer cells. For the treated group, cancer cells were cultured with BPNSs@CD146Ab for 12 h, treated with an 808 nm laser for 5 min, and subsequently returned into the cell incubator for another 12 h. PFQNM-LC-A-CAL probes (rip radius: 65 nm) were used for nanomechanical imaging, with a 300−600 nm vertical oscillation at a frequency of 0.25 kHz and an 800−1000 pN indent force. A single live cell was imaged in the cell medium at 37 °C using a frequency of 0.12 Hz and 256 × 256 pixels. NanoScope Analysis (v1.9, Bruker) software was used to analyze AFM images and indent curves.

dSTORM Imaging. Cancer cells were treated with BPNSs@CD146Ab + laser and then returned to the 37 °C cell incubator for another 12 h, followed by fixation with 4% PFA, permeabilization with cytoskeletal buffer (0.1% Triton X-100), background deduction with 0.1% sodium borohydride, and blocking with BlockAid blocking solution (Thermo Fisher). Next, the fixed cells were stained with 66 μM AlexaFluor-568-phalloidin (Thermo Fisher) in PBS under 4 °C for 12 h, and washed with DPBS. The buffer for dSTORM was added to cell sample prior to dSTORM imaging and was changed each hour. Instrumentation details for dSTORM imaging, and the components for cytoskeletal buffer and imaging buffer can be found in our earlier publication.[42] The data was processed through ImageJ and ThunderSTORM.

Western Blotting. The Mem-PER Plus Membrane Protein Extraction Kit (Thermo Fisher, 89842) was utilized to extract membrane protein CD146. Active Rho Kit (Thermo Fisher, 16116) was used to isolate and detect RhoA-GTP. RIPA buffer (Thermo Fisher, 89901) was used for the extraction of EMT proteins (E-cadherin, N-cadherin, cytokeratin, and vimentin), ERM, and p-ERM proteins, Snail and Slug. The concentration of total protein was measured using a BCA assay (Thermo Fisher, 23225). The same amount of protein was loaded to an SDS-PAGE gel (4−20%) for electrophoresis. Then the gel was processed following the below protocols: the protein was transferred to the nitrocellulose membrane, blocking with EveryBlot blocking buffer (Bio-Rad), incubating with a primary antibody, incubating with a secondary antibody, developing with ECL Western blotting substrates (Bio-Rad), and imaging with ChemiDoc imager (Bio-Rad) after several times of washing. All antibodies for the Western blot analysis are listed in Table 1 in the Supporting Information.

ASSOCIATED CONTENT

Supporting Information

The Supporting Information is available free of charge at https://pubs.acs.org/doi/10.1021/acsnano.1c11070.

> Table 1, listing antibodies used in Western blotting; and Figure S1−S25, showing estimation of protein numbers on single BPNS; TEM images of BPNSs@CD146Ab; colloidal, material, photothermal, and coating stability of BPNSs@CD146Ab; immunofluorescence staining of cell surface CD146; complete data sets of cell uptake, cytotoxicity, and migration assays; and nanomechanical and super-resolution imaging of single cells, along with statistical analysis of the images (PDF)

AUTHOR INFORMATION

Corresponding Author

Congzhou Wang − *Nanoscience and Nanoengineering, South Dakota School of Mines and Technology, Rapid City, South Dakota 57701, United States; BioSystems Networks & Translational Research (BioSNTR), Rapid City, South Dakota 57701, United States;* orcid.org/0000-0001-6132-447X; Email: congzhou.wang@sdsmt.edu

Authors

Jinyuan Liu − *Nanoscience and Nanoengineering, South Dakota School of Mines and Technology, Rapid City, South Dakota 57701, United States; BioSystems Networks & Translational Research (BioSNTR), Rapid City, South Dakota 57701, United States*

Steve Smith − *Nanoscience and Nanoengineering, South Dakota School of Mines and Technology, Rapid City, South Dakota 57701, United States; BioSystems Networks & Translational Research (BioSNTR), Rapid City, South Dakota 57701, United States*

Complete contact information is available at: https://pubs.acs.org/10.1021/acsnano.1c11070

Notes

The authors declare no competing financial interest.

ACKNOWLEDGMENTS

This work was funded by the National Science Foundation CAREER Award (Award number: 2143972) and the South Dakota Board of Regents using the Competitive Research Grant and the Biomaterials Collaboratory (IMAGEN).

REFERENCES

(1) Chaffer, C. L.; Weinberg, R. A. A Perspective on Cancer Cell Metastasis. *Science* **2011**, *331*, 1559−1564.

(2) Fidler, I. J. The Pathogenesis of Cancer Metastasis: the 'Seed and Soil' Hypothesis Revisited. *Nat. Rev. Cancer* **2003**, *3*, 453−8.

(3) Yang, J.; Antin, P.; Berx, G.; Blanpain, C.; Brabletz, T.; Bronner, M.; Campbell, K.; Cano, A.; Casanova, J.; Christofori, G.; Dedhar, S.; Derynck, R.; Ford, H. L.; Fuxe, J.; García de Herreros, A.; Goodall, G. J.; Hadjantonakis, A.-K.; Huang, R. J. Y.; Kalcheim, C.; Kalluri, R.; et al. Guidelines and Definitions for Research on Epithelial-Mesenchymal Transition. *Nat. Rev. Mol. Cell Biol.* **2020**, *21*, 341−352.

(4) Thiery, J. P.; Acloque, H.; Huang, R. Y.; Nieto, M. A. Epithelial-Mesenchymal Transitions in Development and Disease. *Cell* **2009**, *139*, 871−90.

(5) Nieto, M. A.; Huang, R. Y.-J.; Jackson, R. A.; Thiery, J. P. EMT: 2016. *Cell* **2016**, *166*, 21−45.

(6) Marcucci, F.; Stassi, G.; De Maria, R. Epithelial-Mesenchymal Transition: a New Target in Anticancer Drug Discovery. *Nat. Rev. Drug Discovery* **2016**, *15*, 311−25.

(7) Jonckheere, S.; Adams, J.; De Groote, D.; Campbell, K.; Berx, G.; Goossens, S. Epithelial-Mesenchymal Transition (EMT) as a Therapeutic Target. *Cells, tissues, organs* **2021**, 1−26.

(8) Zou, L.; Wang, H.; He, B.; Zeng, L.; Tan, T.; Cao, H.; He, X.; Zhang, Z.; Guo, S.; Li, Y. Current Approaches of Photothermal Therapy in Treating Cancer Metastasis with Nanotherapeutics. *Theranostics* **2016**, *6*, 762−772.

(9) Jin, C. S.; Lovell, J. F.; Chen, J.; Zheng, G. Ablation of Hypoxic Tumors with Dose-Equivalent Photothermal, but Not Photodynamic, Therapy Using a Nanostructured Porphyrin Assembly. *ACS Nano* **2013**, *7*, 2541−2550.

(10) Gao, G.; Jiang, Y. W.; Sun, W.; Guo, Y.; Jia, H. R.; Yu, X. W.; Pan, G. Y.; Wu, F. G. Molecular Targeting-Mediated Mild-Temperature Photothermal Therapy with a Smart Albumin-Based Nanodrug. *Small* **2019**, *15*, No. e1900501.

(11) Pérez-Hernández, M.; Del Pino, P.; Mitchell, S. G.; Moros, M.; Stepien, G.; Pelaz, B.; Parak, W. J.; Gálvez, E. M.; Pardo, J.; de la Fuente, J. M. Dissecting the Molecular Mechanism of Apoptosis during Photothermal Therapy Using Gold Nanoprisms. *ACS Nano* **2015**, *9*, 52−61.

(12) Wang, H.; Chang, J.; Shi, M.; Pan, W.; Li, N.; Tang, B. A Dual-Targeted Organic Photothermal Agent for Enhanced Photothermal Therapy. *Angew. Chem., Int. Ed.* **2019**, *58*, 1057−1061.

(13) Li, N.; Sun, Q.; Yu, Z.; Gao, X.; Pan, W.; Wan, X.; Tang, B. Nuclear-Targeted Photothermal Therapy Prevents Cancer Recurrence with Near-Infrared Triggered Copper Sulfide Nanoparticles. *ACS Nano* **2018**, *12*, 5197−5206.
(14) Wu, Y.; Ali, M. R. K.; Dong, B.; Han, T.; Chen, K.; Chen, J.; Tang, Y.; Fang, N.; Wang, F.; El-Sayed, M. A. Gold Nanorod Photothermal Therapy Alters Cell Junctions and Actin Network in Inhibiting Cancer Cell Collective Migration. *ACS Nano* **2018**, *12*, 9279−9290.
(15) Zhang, M.; Wang, W.; Mohammadniaei, M.; Zheng, T.; Zhang, Q.; Ashley, J.; Liu, S.; Sun, Y.; Tang, B. Z. Upregulating Aggregation-Induced-Emission Nanoparticles with Blood-Tumor-Barrier Permeability for Precise Photothermal Eradication of Brain Tumors and Induction of Local Immune Responses. *Adv. Mater.* **2021**, *33*, 2008802.
(16) Song, N.; Zhang, Z.; Liu, P.; Dai, D.; Chen, C.; Li, Y.; Wang, L.; Han, T.; Yang, Y.-W.; Wang, D.; Tang, B. Z. Pillar[5]arene-Modified Gold Nanorods as Nanocarriers for Multi-Modal Imaging-Guided Synergistic Photodynamic-Photothermal Therapy. *Adv. Funct. Mater.* **2021**, *31*, 2009924.
(17) Li, X.; Sun, H.; Li, H.; Hu, C.; Luo, Y.; Shi, X.; Pich, A. Multi-Responsive Biodegradable Cationic Nanogels for Highly Efficient Treatment of Tumors. *Adv. Funct. Mater.* **2021**, *31*, 2100227.
(18) Veeranarayanan, S.; Mohamed, M. S.; Poulose, A. C.; Rinya, M.; Sakamoto, Y.; Maekawa, T.; Kumar, D. S. Photodynamic Therapy at Ultra-Low NIR Laser Power and X-Ray Imaging Using Cu(3)-BiS(3) Nanocrystals. *Theranostics* **2018**, *8*, 5231−5245.
(19) Shi, M.; Fu, Z.; Pan, W.; Chen, Y.; Wang, K.; Zhou, P.; Li, N.; Tang, B. A Protein-Binding Molecular Photothermal Agent for Tumor Ablation. *Angew. Chem., Int. Ed.* **2021**, *60*, 13564−13568.
(20) Johnson, J. P. Cell Adhesion Molecules in the Development and Progression of Malignant Melanoma. *Cancer Metastasis Rev.* **1999**, *18*, 345−357.
(21) Wang, Z.; Yan, X. CD146, a Multi-Functional Molecule beyond Adhesion. *Cancer Lett.* **2013**, *330*, 150−162.
(22) Luo, Y.; Zheng, C.; Zhang, J.; Lu, D.; Zhuang, J.; Xing, S.; Feng, J.; Yang, D.; Yan, X. Recognition of CD146 as an ERM-Binding Protein Offers Novel Mechanisms for Melanoma Cell Migration. *Oncogene* **2012**, *31*, 306−21.
(23) Zabouo, G.; Imbert, A. M.; Jacquemier, J.; Finetti, P.; Moreau, T.; Esterni, B.; Birnbaum, D.; Bertucci, F.; Chabannon, C. CD146 Expression is Associated with a Poor Prognosis in Human Breast Tumors and with Enhanced Motility in Breast Cancer Cell Lines. *Breast Cancer Res.* **2009**, *11*, R1.
(24) Zoni, E.; Astrologo, L.; Ng, C. K. Y.; Piscuoglio, S.; Melsen, J.; Grosjean, J.; Klima, I.; Chen, L.; Snaar-Jagalska, E. B.; Flanagan, K.; van der Pluijm, G.; Kloen, P.; Cecchini, M. G.; Kruithof-de Julio, M.; Thalmann, G. N. Therapeutic Targeting of CD146/MCAM Reduces Bone Metastasis in Prostate Cancer. *Mol. Cancer Res.* **2019**, *17*, 1049−1062.
(25) Zhou, P.; Xiong, T.; Chen, J.; Li, F.; Qi, T.; Yuan, J. Clinical Significance of Melanoma Cell Adhesion Molecule CD146 and VEGFA Expression in Epithelial Ovarian Cancer. *Oncol. Lett.* **2019**, *17*, 2418−2424.
(26) Wang, Z.; Xu, Q.; Zhang, N.; Du, X.; Xu, G.; Yan, X. CD146, from a Melanoma Cell Adhesion Molecule to a Signaling Receptor. *Signal Transduction Targeted Ther.* **2020**, *5*, 148.
(27) Zeng, Q.; Li, W.; Lu, D.; Wu, Z.; Duan, H.; Luo, Y.; Feng, J.; Yang, D.; Fu, L.; Yan, X. CD146, an Epithelial-Mesenchymal Transition Inducer, is Associated with Triple-Negative Breast Cancer. *Proc. Natl. Acad. Sci. U. S. A.* **2012**, *109*, 1127−32.
(28) Lamouille, S.; Xu, J.; Derynck, R. Molecular Mechanisms of Epithelial-Mesenchymal Transition. *Nat. Rev. Mol. Cell Biol.* **2014**, *15*, 178−196.
(29) Huang, J.; He, B.; Zhang, Z.; Li, Y.; Kang, M.; Wang, Y.; Li, K.; Wang, D.; Tang, B. Z. Aggregation-Induced Emission Luminogens Married to 2D Black Phosphorus Nanosheets for Highly Efficient Multimodal Theranostics. *Adv. Mater.* **2020**, *32*, 2003382.
(30) Chan, L.; Chen, X.; Gao, P.; Xie, J.; Zhang, Z.; Zhao, J.; Chen, T. Coordination-Driven Enhancement of Radiosensitization by Black Phosphorus via Regulating Tumor Metabolism. *ACS Nano* **2021**, *15*, 3047−3060.
(31) Liu, W.; Dong, A.; Wang, B.; Zhang, H. Current Advances in Black Phosphorus-Based Drug Delivery Systems for Cancer Therapy. *Adv. Sci.* **2021**, *8*, 2003033.
(32) Zhu, J.; Li, B.; Xu, M.; Liu, R.; Xia, T.; Zhang, Z.; Xu, Y.; Liu, S. Graphene Oxide Promotes Cancer Metastasis through Associating with Plasma Membrane to Promote TGF-β Signaling-Dependent Epithelial-Mesenchymal Transition. *ACS Nano* **2020**, *14*, 818−827.
(33) Tripathi, K.; Driskell, J. D. Quantifying Bound and Active Antibodies Conjugated to Gold Nanoparticles: A Comprehensive and Robust Approach to Evaluate Immobilization Chemistry. *ACS Omega* **2018**, *3*, 8253−8259.
(34) Luan, J.; Seth, A.; Gupta, R.; Wang, Z.; Rathi, P.; Cao, S.; Gholami Derami, H.; Tang, R.; Xu, B.; Achilefu, S.; Morrissey, J. J.; Singamaneni, S. Ultrabright Fluorescent Nanoscale Labels for the Femtomolar Detection of Analytes with Standard Bioassays. *Nat. Biomed. Eng.* **2020**, *4*, 518−530.
(35) Guo, Z.; Zhang, H.; Lu, S.; Wang, Z.; Tang, S.; Shao, J.; Sun, Z.; Xie, H.; Wang, H.; Yu, X.-F.; Chu, P. K. Phosphorene: From Black Phosphorus to Phosphorene: Basic Solvent Exfoliation, Evolution of Raman Scattering, and Applications to Ultrafast Photonics. *Adv. Funct. Mater.* **2015**, *25*, 7100−7100.
(36) Luo, M.; Fan, T.; Zhou, Y.; Zhang, H.; Mei, L. 2D Black Phosphorus-Based Biomedical Applications. *Adv. Funct. Mater.* **2019**, *29*, 1808306.
(37) Mo, J.; Xie, Q.; Wei, W.; Zhao, J. Revealing the Immune Perturbation of Black Phosphorus Nanomaterials to Macrophages by Understanding the Protein Corona. *Nat. Commun.* **2018**, *9*, 2480.
(38) Eteshola, E.; Keener, M. T.; Elias, M.; Shapiro, J.; Brillson, L. J.; Bhushan, B.; Lee, S. C. Engineering Functional Protein Interfaces for Immunologically Modified Field Effect Transistor (ImmunoFET) by Molecular Genetic Means. *J. R. Soc. Interface* **2008**, *5*, 123−127.
(39) Tao, W.; Zhu, X.; Yu, X.; Zeng, X.; Xiao, Q.; Zhang, X.; Ji, X.; Wang, X.; Shi, J.; Zhang, H.; Mei, L. Black Phosphorus Nanosheets as a Robust Delivery Platform for Cancer Theranostics. *Adv. Mater.* **2017**, *29*, 1603276.
(40) Chen, W.; Ouyang, J.; Liu, H.; Chen, M.; Zeng, K.; Sheng, J.; Liu, Z.; Han, Y.; Wang, L.; Li, J.; Deng, L.; Liu, Y.-N.; Guo, S. Black Phosphorus Nanosheet-Based Drug Delivery System for Synergistic Photodynamic/Photothermal/Chemotherapy of Cancer. *Adv. Mater.* **2017**, *29*, 1603864.
(41) Shao, J.; Ruan, C.; Xie, H.; Li, Z.; Wang, H.; Chu, P. K.; Yu, X.-F. Black-Phosphorus-Incorporated Hydrogel as a Sprayable and Biodegradable Photothermal Platform for Postsurgical Treatment of Cancer. *Adv. Sci.* **2018**, *5*, 1700848.
(42) Kota, D.; Kang, L.; Rickel, A.; Liu, J.; Smith, S.; Hong, Z.; Wang, C. Low Doses of Zeolitic Imidazolate Framework-8 Nanoparticles Alter the Actin Organization and Contractility of Vascular Smooth Muscle Cells. *J. Hazard. Mater.* **2021**, *414*, 125514.
(43) Majzoub, R. N.; Wonder, E.; Ewert, K. K.; Kotamraju, V. R.; Teesalu, T.; Safinya, C. R. Rab11 and Lysotracker Markers Reveal Correlation between Endosomal Pathways and Transfection Efficiency of Surface-Functionalized Cationic Liposome-DNA Nanoparticles. *J. Phys. Chem. B* **2016**, *120*, 6439−6453.
(44) Sun, Q.; Kanehira, K.; Taniguchi, A. PEGylated TiO(2) Nanoparticles Mediated Inhibition of Cell Migration via Integrin Beta 1. *Sci. Technol. Adv. Mater.* **2018**, *19*, 271−281.
(45) Imbert, A.-M.; Garulli, C.; Choquet, E.; Koubi, M.; Aurrand-Lions, M.; Chabannon, C. CD146 Expression in Human Breast Cancer Cell Lines Induces Phenotypic and Functional Changes Observed in Epithelial to Mesenchymal Transition. *PloS one* **2012**, *7*, No. e43752.
(46) Jonkman, J. E. N.; Cathcart, J. A.; Xu, F.; Bartolini, M. E.; Amon, J. E.; Stevens, K. M.; Colarusso, P. An Introduction to the Wound Healing Assay Using Live-Cell Microscopy. *Cell Adhes. Migr.* **2014**, *8*, 440−451.

https://doi.org/10.1021/acsnano.1c11070
ACS Nano XXXX, XXX, XXX−XXX

(47) Xiong, Z.; Alves, C. S.; Wang, J.; Li, A.; Liu, J.; Shen, M.; Rodrigues, J.; Tomás, H.; Shi, X. Zwitterion-Functionalized Dendrimer-Entrapped Gold Nanoparticles for Serum-Enhanced Gene Delivery to Inhibit Cancer Cell Metastasis. *Acta Biomater.* **2019**, *99*, 320−329.
(48) Zaman, M. H.; Trapani, L. M.; Sieminski, A. L.; MacKellar, D.; Gong, H.; Kamm, R. D.; Wells, A.; Lauffenburger, D. A.; Matsudaira, P. Migration of Tumor Cells in 3D Matrices is Governed by Matrix Stiffness along with Cell-Matrix Adhesion and Proteolysis. *Proc. Natl. Acad. Sci. U. S. A.* **2006**, *103*, 10889.
(49) Yang, J. A.; Phan, H. T.; Vaidya, S.; Murphy, C. J. Nanovacuums: Nanoparticle Uptake and Differential Cellular Migration on a Carpet of Nanoparticles. *Nano Lett.* **2013**, *13*, 2295−2302.
(50) Zhou, T.; Yu, M.; Zhang, B.; Wang, L.; Wu, X.; Zhou, H.; Du, Y.; Hao, J.; Tu, Y.; Chen, C.; Wei, T. Inhibition of Cancer Cell Migration by Gold Nanorods: Molecular Mechanisms and Implications for Cancer Therapy. *Adv. Funct. Mater.* **2014**, *24*, 6922−6932.
(51) Ali, M. R. K.; Wu, Y.; Tang, Y.; Xiao, H.; Chen, K.; Han, T.; Fang, N.; Wu, R.; El-Sayed, M. A. Targeting Cancer Cell Integrins Using Gold Nanorods in Photothermal Therapy Inhibits Migration through Affecting Cytoskeletal Proteins. *Proc. Natl. Acad. Sci. U. S. A.* **2017**, *114*, E5655−E5663.
(52) Olson, M. F.; Sahai, E. The Actin Cytoskeleton in Cancer Cell Motility. *Clin. Exp. Metastasis* **2009**, *26*, 273−287.
(53) Wang, M.; Cheng, B.; Yang, Y.; Liu, H.; Huang, G.; Han, L.; Li, F.; Xu, F. Microchannel Stiffness and Confinement Jointly Induce the Mesenchymal-Amoeboid Transition of Cancer Cell Migration. *Nano Lett.* **2019**, *19*, 5949−5958.
(54) Huang, G.; Xu, F.; Genin, G. M.; Lu, T. J. Mechanical Microenvironments of Living Cells: a Critical Frontier in Mechanobiology. *Acta Mech. Sin.* **2019**, *35*, 265−269.
(55) Dumitru, A. C.; Poncin, M. A.; Conrard, L.; Dufrene, Y. F.; Tyteca, D.; Alsteens, D. Nanoscale Membrane Architecture of Healthy and Pathological Red Blood Cells. *Nanoscale Horiz.* **2018**, *3*, 293−304.
(56) Eghiaian, F.; Rigato, A.; Scheuring, S. Structural, Mechanical, and Dynamical Variability of the Actin Cortex in Living Cells. *Biophys. J.* **2015**, *108*, 1330−1340.
(57) Calzado-Martín, A.; Encinar, M.; Tamayo, J.; Calleja, M.; San Paulo, A. Effect of Actin Organization on the Stiffness of Living Breast Cancer Cells Revealed by Peak-Force Modulation Atomic Force Microscopy. *ACS Nano* **2016**, *10*, 3365−3374.
(58) Vallenius, T. Actin Stress Fibre Subtypes in Mesenchymal-Migrating Cells. *Open Biol.* **2013**, *3*, 130001−130001.
(59) Kurland, N. E.; Drira, Z.; Yadavalli, V. K. Measurement of Nanomechanical Properties of Biomolecules Using Atomic Force Microscopy. *Micron* **2012**, *43*, 116−28.
(60) Van de Linde, S.; Löschberger, A.; Klein, T.; Heidbreder, M.; Wolter, S.; Heilemann, M.; Sauer, M. Direct Stochastic Optical Reconstruction Microscopy with Standard Fluorescent Probes. *Nat. Protoc.* **2011**, *6*, 991−1009.
(61) Dempsey, G. T.; Vaughan, J. C.; Chen, K. H.; Bates, M.; Zhuang, X. Evaluation of Fluorophores for Optimal Performance in Localization-Based Super-Resolution Imaging. *Nat. Methods* **2011**, *8*, 1027−1036.
(62) Xu, J.; Ma, H.; Liu, Y. Stochastic Optical Reconstruction Microscopy (STORM). *Curr. Protoc. Cytom.* **2017**, *81*, 12.46.1−12.46.27.
(63) Sun, B. O.; Fang, Y.; Li, Z.; Chen, Z.; Xiang, J. Role of Cellular Cytoskeleton in Epithelial-Mesenchymal Transition Process during Cancer Progression. *Biomed. Rep.* **2015**, *3*, 603−610.
(64) Zhang, C.; Zhu, H.; Ren, X.; Gao, B.; Cheng, B.; Liu, S.; Sha, B.; Li, Z.; Zhang, Z.; Lv, Y.; Wang, H.; Guo, H.; Lu, T. J.; Xu, F.; Genin, G. M.; Lin, M. Mechanics-Driven Nuclear Localization of YAP Can be Reversed by N-Cadherin Ligation in Mesenchymal Stem Cells. *Nat. Commun.* **2021**, *12*, 6229.
(65) Furukawa, K. T.; Yamashita, K.; Sakurai, N.; Ohno, S. The Epithelial Circumferential Actin Belt Regulates YAP/TAZ through Nucleocytoplasmic Shuttling of Merlin. *Cell Rep.* **2017**, *20*, 1435−1447.
(66) Bosch-Fortea, M.; Martín-Belmonte, F. Mechanosensitive Adhesion Complexes in Epithelial Architecture and Cancer Onset. *Curr. Opin. Cell Biol.* **2018**, *50*, 42−49.
(67) Lorentzen, A.; Becker, P. F.; Kosla, J.; Saini, M.; Weidele, K.; Ronchi, P.; Klein, C.; Wolf, M. J.; Geist, F.; Seubert, B.; Ringelhan, M.; Mihic-Probst, D.; Esser, K.; Roblek, M.; Kuehne, F.; Bianco, G.; O'Connor, T.; Müller, Q.; Schuck, K.; Lange, S.; et al. Single Cell Polarity in Liquid Phase Facilitates Tumour Metastasis. *Nat. Commun.* **2018**, *9*, 887.
(68) Zhang, Z.; Wang, J.; Shanmugasundaram, K. B.; Yeo, B.; Möller, A.; Wuethrich, A.; Lin, L. L.; Trau, M. Tracking Drug-Induced Epithelial-Mesenchymal Transition in Breast Cancer by a Microfluidic Surface-Enhanced Raman Spectroscopy Immunoassay. *Small* **2020**, *16*, No. e1905614.
(69) Xie, F.; Shao, S.; Aziz, A. U. R.; Zhang, B.; Wang, H.; Liu, B. Role of Rho-Specific Guanine Nucleotide Dissociation Inhibitor α Regulation in Cell Migration. *Acta Histochem.* **2017**, *119*, 183−189.
(70) Lei, X.; Guan, C.-W.; Song, Y.; Wang, H. The Multifaceted Role of CD146/MCAM in the Promotion of Melanoma Progression. *Cancer Cell Int.* **2015**, *15*, 3.
(71) Dharmasiri, S.; Harrington, H. M.; Dharmasiri, N. Heat Shock Modulates Phosphorylation Status and Activity of Nucleoside Diphosphate Kinase in Cultured Sugarcane Cells. *Plant Cell Rep.* **2010**, *29*, 1305−14.
(72) Duncan, R. F.; Hershey, J. W. Protein Synthesis and Protein Phosphorylation during Heat Stress, Recovery, and Adaptation. *J. Cell Biol.* **1989**, *109*, 1467−81.
(73) Wang, Z.; Xia, F.; Labib, M.; Ahmadi, M.; Chen, H.; Das, J.; Ahmed, S. U.; Angers, S.; Sargent, E. H.; Kelley, S. O. Nanostructured Architectures Promote the Mesenchymal-Epithelial Transition for Invasive Cells. *ACS Nano* **2020**, *14*, 5324−5336.
(74) Alves, C. C.; Carneiro, F.; Hoefler, H.; Becker, K. F. Role of the Epithelial-Mesenchymal Transition Regulator Slug in Primary Human Cancers. *Front. Biosci., Elite Ed.* **2009**, *14*, 3035−3050.
(75) Shankar, J.; Nabi, I. R. Actin Cytoskeleton Regulation of Epithelial Mesenchymal Transition in Metastatic Cancer Cells. *PloS one* **2015**, *10*, No. e0119954.
(76) Leong, K. G.; Niessen, K.; Kulic, I.; Raouf, A.; Eaves, C.; Pollet, I.; Karsan, A. Jagged1-Mediated Notch Activation Induces Epithelial-to-Mesenchymal Transition through Slug-Induced Repression of E-Cadherin. *J. Exp. Med.* **2007**, *204*, 2935−48.
(77) Alifu, N.; Zebibula, A.; Qi, J.; Zhang, H.; Sun, C.; Yu, X.; Xue, D.; Lam, J. W. Y.; Li, G.; Qian, J.; Tang, B. Z. Single-Molecular Near-Infrared-II Theranostic Systems: Ultrastable Aggregation-Induced Emission Nanoparticles for Long-Term Tracing and Efficient Photothermal Therapy. *ACS Nano* **2018**, *12*, 11282−11293.
(78) Seth, A.; Gholami Derami, H.; Gupta, P.; Wang, Z.; Rathi, P.; Gupta, R.; Cao, T.; Morrissey, J. J.; Singamaneni, S. Polydopamine-Mesoporous Silica Core-Shell Nanoparticles for Combined Photothermal Immunotherapy. *ACS Appl. Mater. Interfaces* **2020**, *12*, 42499−42510.
(79) Jiang, R.; Dai, J.; Dong, X.; Wang, Q.; Meng, Z.; Guo, J.; Yu, Y.; Wang, S.; Xia, F.; Zhao, Z.; Lou, X.; Tang, B. Z. Improving Image-Guided Surgical and Immunological Tumor Treatment Efficacy by Photothermal and Photodynamic Therapies Based on a Multifunctional NIR AIEgen. *Adv. Mater.* **2021**, *33*, 2101158.
(80) Hu, W.; Xiao, T.; Li, D.; Fan, Y.; Xing, L.; Wang, X.; Li, Y.; Shi, X.; Shen, M. Intelligent Molybdenum Disulfide Complexes as a Platform for Cooperative Imaging-Guided Tri-Mode Chemo-Photothermo-Immunotherapy. *Adv. Sci.* **2021**, *8*, 2100165.
(81) Du, B.; Shim, J. S. Targeting Epithelial-Mesenchymal Transition (EMT) to Overcome Drug Resistance in Cancer. *Molecules* **2016**, *21*, 965.
(82) Shibue, T.; Weinberg, R. A. EMT, CSCs, and Drug Resistance: the Mechanistic Link and Clinical Implications. *Nat. Rev. Clin. Oncol.* **2017**, *14*, 611−629.

https://doi.org/10.1021/acsnano.1c11070
ACS Nano XXXX, XXX, XXX−XXX